# In Situ Raman Study of Phase Stability of α-Li$_3$V$_2$(PO$_4$)$_3$ upon Thermal and Laser Heating

Nellymar Membreño,[†] Penghao Xiao,[†] Kyu-Sung Park,[‡,∥] John B. Goodenough,[‡,§,∥] Graeme Henkelman,*,[†] and Keith J. Stevenson*,[†,§,∥]

[†]Department of Chemistry and Biochemistry (105 E. 24th St. Stop A5300), [‡]Materials Science and Engineering Program, [§]Center for Electrochemistry, and [∥]Texas Materials Institute, The University of Texas at Austin, Austin, Texas 78712, United States

S *Supporting Information*

ABSTRACT: Monoclinic α-Li$_3$V$_2$(PO$_4$)$_3$ has a complex 3-D metal phosphate framework that provides mobility for all three lithium ions, giving it the highest gravimetric capacity (197 mAh/g) of all the transition-metal phosphates. Along with its high gravimetric capacity, its thermal and electrochemical stability make it of great interest as a cathode material for lithium-ion energy storage devices. Raman spectroscopy has proven to be a unique analytical tool for studying electrode materials of lithium-ion batteries due to its ability to probe structural changes at the level of chemical bonds. In this work, the calculated Raman spectrum of α-Li$_3$V$_2$(PO$_4$)$_3$ provided by density functional theory is presented along with symmetry assignments for all of the calculated and observed modes through Raman microscopy. Furthermore, the phase stability of microcrystalline α-Li$_3$V$_2$(PO$_4$)$_3$ was studied as a function of irradiation power density. Follow-up thermal studies confirm that two structural phase transitions, β and γ, occur at elevated temperatures or high irradiation power density before degradation to α-LiVOPO$_4$ under an oxygen-rich atmosphere. Calculated and experimentally determined Raman modes for α-Li$_3$V$_2$(PO$_4$)$_3$ are in good agreement. It is also noted that careful consideration of the irradiation power density employed must be taken into account to prevent misinterpretation of Raman spectral features.
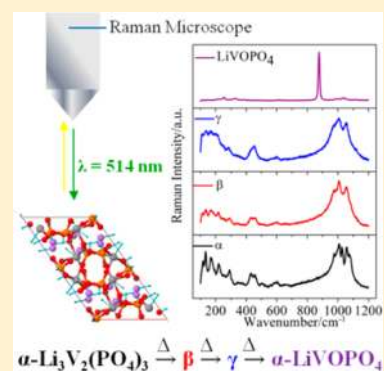
1. INTRODUCTION

Transition-metal phosphates that include LiFePO$_4$, LiMnPO$_4$, and Li$_3$V$_2$(PO$_4$)$_3$ have resurged as alternatives to the commercially dominating LiCoO$_2$ cathode owing to their safety, thermal stability, low cost, and competitive energy densities.[1,2] The inherent stability of these materials originates from the P–O bond covalency in the metal phosphate framework that houses mobile Li ions.[1] Li$_3$V$_2$(PO$_4$)$_3$ can be found in either the rhombohedral (NASICON) or the monoclinic (α) lattice system at room temperature, depending on the synthetic route, with the latter phase being the more thermodynamically stable.[2]

In the monoclinic lattice, the V$_2$(PO$_4$)$_3$ units are alternately positioned perpendicular to one another, creating a slightly more compressed structure as compared to the rhombohedral phase.[3] More specifically, two distinct vanadium sites are present in slightly distorted VO$_6$ octahedra that share oxygen vertices with PO$_4$ tetrahedra (the three phosphate tetrahedra can be distinguished by their varying average P–O bond lengths).[2] Within the interstitial voids of the lattice are three unique lithium sites. Following the assignment used by Yin et al., Li(1) is coordinated to four oxygens, forming a true tetrahedron, while Li(2) and Li(3) occupy a highly distorted tetrahedron with a fifth Li–O bond.[2] Along the a axis of the crystal, Li polyhedra are linked through common oxygen, allowing for diffusion along the other directions.[3] However, Lee et al. calculated lower migration energies along the [001]

direction, resulting in a highly anisotropic Li$^+$ mobility despite not being one-dimensional.[4] Nevertheless, the ability to electrochemically extract all three lithium ions from α-Li$_3$V$_2$(PO$_4$)$_3$ gives it the high specific gravimetric capacity of 197 mAh/g. This value is the highest of all the transition-metal phosphates, making it a prospective cathode material for lithium-ion batteries and meriting a fundamental understanding of its vibrational modes through Raman microscopy.

Raman microscopy is highly suitable for probing the chemical bond structure in electrode materials used in lithium-ion energy storage devices. The microscope offers the ability to focus the photon beam onto a small area (~1 μm diameter) of importance for electrode materials that are composite mixtures of conductive carbon (to enhance electronic conductivity) and binder.[5] Raman microscopy frequently serves as a complementary technique to X-ray diffraction (XRD)[6] and powder neutron diffraction (PND) data for crystalline materials. However, unlike diffraction methods that solely identify materials with long-range order, Raman spectroscopy allows for the investigation of amorphous materials.[5] On a more technical level, there is no need for a particular sample preparation and the excitation source is chosen to be nondestructive. Consequently, little to no

modifications are made to the sample, permitting it to be further analyzed by other techniques.[5]

From an analytical perspective, Raman microscopy provides the high sensitivity necessary to detect changes in crystal symmetry, oxidation states, local phase inhomogeneities, and structural order/disorder.[5] This sensitivity is especially useful for ex situ analysis of cycled electrodes.[5,7] Moreover, in situ measurements can be easily devised by using transparent materials (such as glass, quartz, and sapphire) as optical windows for electrochemical cells as they present too weak a Raman signal to cause interference.[8−10] These spectroelectrochemical devices have served as invaluable tools for understanding lithium intercalation mechanisms in both cathode and anode materials as well as for the understanding of the chemical and/or electrochemical processes that are responsible for cell failure.[5]

Although structural characterization of transition-metal phosphates has predominantly been executed via Li[7] magic-angle spinning nuclear magnetic resonance (MAS NMR),[11,12] Mossbauer spectroscopy, and PND,[13] a number of optical spectroscopy studies have been reported for these materials.[14−17] The commercial success of the cheap and toxically benign LiFePO$_4$ has made it the most thoroughly studied of the phosphates.[1] Burba et al.[14] observed Raman spectral changes of chemically delithiated LiFePO$_4$ ($0 \leq x \leq 1$). With partial delithiation (Li$_{0.74}$FePO$_4$), new spectral peaks were found in the ν_1 and ν_3 region of the spectrum that grew in intensity until complete delithiation (FePO$_4$). Despite not having complete assignments of the vibrations, these observations provided indirect evidence of the two-phase mechanism for the electrochemical delithiation of LiFePO$_4$. Paraguassu et al.[18] later assigned all 36 Raman wavenumbers for LiFePO$_4$ using a computational simulation based on Wilson's FG matrix method. The method was applied to LiFePO$_4$ and LiNiPO$_4$. It showed good agreement between experimental and calculated wavenumbers (about 5% and 9% deviation, respectively).

Li$_3$M$_2$(PO$_4$)$_3$ (M = Sc, Fe) compounds, isostructural to Li$_3$V$_2$(PO$_4$)$_3$, were investigated by Kravchenko et al.[17] by means of infrared (IR) and Raman microscopy in the 77−670 K temperature range to understand the structural changes associated with the superionic phase transition.[7] Complete spectral assignments were not made in these studies, but identification of the sublattice lithium vibrations, found at 505 cm^{-1} in the Raman spectrum of Li$_3$Sc$_2$(PO$_4$)$_3$, was made by comparison of Li[6] isotope enriched Li$_3$Sc$_2$(PO$_4$)$_3$ with a nonenriched sample. Burba et al.[7] later looked at vibrations for the electrochemically delithiated species ($0 \leq x \leq 3$) of both NASICON and α-Li$_3$V$_2$(PO$_4$)$_3$ with emphasis on the (PO$_4$)$^{3-}$ vibrations that are highly sensitive to Li$^+$ extraction and the oxidation state of vanadium. Ex situ mid-IR spectra were found to be in accordance with the already established complex two-phase transition mechanism proposed by Yin et al.[2,12] Furthermore, the work showed that, after the first electrochemical cycle, full reversibility of the α-Li$_3$V$_2$(PO$_4$)$_3$ structure is regained with some (PO$_4$)$^{3-}$ band broadening indicative of some local disordering. The investigators intended to similarly analyze the (PO$_4$)$^{3-}$ Raman active vibrations for α-Li$_3$V$_2$(PO$_4$)$_3$ at various electrochemically delithiated stages, but the weak bands observed did not allow for further analysis. The usually intense phosphate peaks were thought to be broadened and weakened because of an amorphous surface layer on the particles.

Here, the complete Raman vibrational spectrum of α-Li$_3$V$_2$(PO$_4$)$_3$ is reported and compared to the theoretical Raman frequencies (wavenumbers) calculated with density functional theory (DFT) using the Vienna ab inito simulation package (VASP). In addition, thermal effects as a function of irradiation power density were studied to understand the phase stability of α-Li$_3$V$_2$(PO$_4$)$_3$ under confocal Raman measurements. Our findings show that, with increasing irradiation power, α-Li$_3$V$_2$(PO$_4$) transforms into the high-temperature β and γ-phases before becoming completely oxidized to LiVOPO$_4$. The oxidation process was further confirmed by thermal studies with both Raman interfaced with a hot-stage and differential scanning calorimetry (DSC).

2. EXPERIMENTAL AND THEORETICAL METHODS

α-Li$_3$V$_2$(PO$_4$)$_3$ Solid State Synthesis. For the preparation of α-Li$_3$V$_2$(PO$_4$)$_3$, stoichiometric amounts of Li$_2$CO$_3$ (Aldrich, >99%), V$_2$O$_3$ (Aldrich, 99.99%), and (NH$_4$)H$_2$PO$_4$ (Alfa Aesar, >98%) were thoroughly mixed in a mortar with the aid of isopropyl alcohol for 1 h. An excess of lithium (2%) was added to compensate for high-temperature lithium evaporation. After thoroughly grinding the precursor materials, the dry mixture was thermally decomposed at 450 °C in an Ar atmosphere for 1 h. The decomposed and oxidized powder was once again ground in a mortar and subsequently pressed into a pellet. Finally, the pellet was heated to 900 °C under a 95% Ar 5% H$_2$ gas flow for 5 h. Upon completion of the calcination process, a green-colored pellet was obtained and ground into a fine powder for materials characterization.

XRD Characterization. Diffraction patterns were collected on a Rigaku R-axis Spider diffractometer equipped with an image plate detector using a Cu Kα radiation source (λ = 1.542 Å) operated at 40 kV and 40 mA. Samples were mounted on a 0.5 mm Nylon loop and scanned for 10 min while rotating at 1°/min. With the 2DP software, radial data were integrated over 2θ = 10−60°. The peaks were analyzed by using the Joint Committee on Powder Diffraction Standards (JCPDS) database.

Environmental Scanning Electron Microscopy (ESEM). Images were obtained with a model Quanta 650 FEG at 30.00 kV.

Ex Situ and In Situ Raman Microscopy. Raman spectra were acquired with a Renishaw inVia microscope system having a 514.5 nm Ar$^+$ laser in the backscattering configuration. For ex situ analysis, the beam was focused with a 50× objective lens, resulting in approximately a 1.3 μm spot diameter under air. The phase stability of Li$_3$V$_2$(PO$_4$)$_3$ under laser irradiation was studied at 0.067, 0.080, 0.113, 0.403, 0.855, 4.101, and 7.612 mW power. The laser was focused on the same sample area while increasing or decreasing the power of the laser. For the in situ heat analysis, under N$_2$ and air, a Linkam Scientific THMS600 microscope stage was used to ramp the sample temperature from room temperature to 600 °C. The temperature program used was as follows: 23−126 °C at a rate of 2 °C/min, 126−150 °C at a rate of 1 °C/min, 150−195 °C at a rate of 2 °C/min, 195−220 °C at a rate of 1 °C/min, and 220−600 °C at a rate of 10 °C/min. One hour temperature holds were performed at 126, 150, 195, and 220 °C, whereas 30 min temperature holds were performed at 258, 296, 334, 372, 410, 448, 486, 524, 562, and 600 °C to ensure complete and homogeneous heating of the sample. The beam was focused with an L 50× objective lens, resulting in approximately a 0.8 μm spot diameter. An acquisition time of about 300 s was used
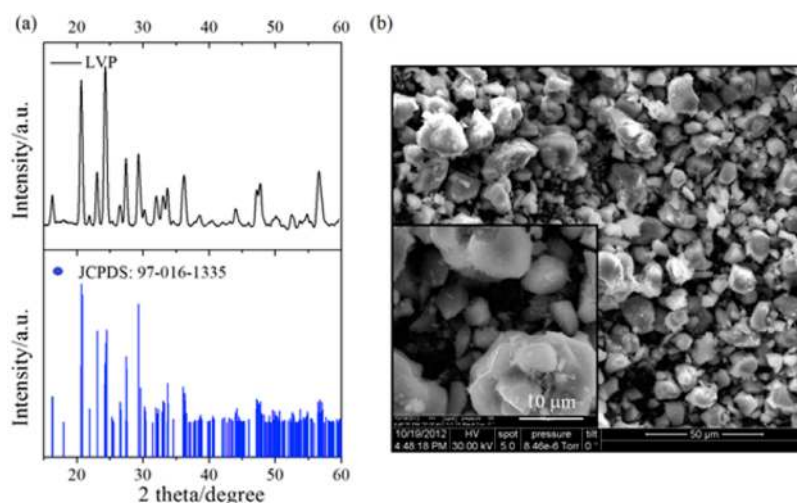
Figure 1. (a) XRD and (b) ESEM of microcrystalline $Li_3V_2(PO_4)_3$.

for the in situ heat analysis and was varied between 20 and 120 s for the ex situ studies.

Thermal Studies. Differential scanning calorimetry (DSC) was conducted on a TA Instruments DSC-Q100. A sample of 9.000 mg was placed in an Al crucible. Each DSC cycle consisted of heating the sample from 25 to 250 °C and then cooling it back to 25 °C. A total of three cycles were performed at a rate of 5 °C/min under a N_2 flow rate of 50.00 mL/min. Thermal gravimetric analysis (TGA) was performed on a TA Instruments TGA-Q50. A sample of 4.347 mg was placed in a Pt crucible. The first ramp consisted of heating the sample from 25 to 500 °C at a rate of 2.50 °C/min. The second ramp continued the heating from 500 to 800 °C at a rate of 5.00 °C/min.

VASP-DFT. The vibrational frequency calculations were performed with finite differences of the atomic forces from DFT,[19] using the HSE06 hybrid functional for the exchange-correlation energy.[20] Valence electrons were described with a plane-wave basis set up to an energy cutoff of 283 eV; core electrons were incorporated into pseudopotentials in the projector augmented wave phasework.[21-24] Only the Γ point was included for the Brillouin-zone integration. The lattice parameters for the crystal supercell were set to experimental values.[2] Tests in which the volume was varied showed that the energy of the experimental lattice constants was very close to the minimum from fitting to the equation of state (0.15 eV higher for 80 atoms). For the frequency calculations, only symmetrically inequivalent forward differences were taken to save computational cost. The magnitude of each displacement was 0.01 Å.

The DFT+U functional was also performed with an effective U value of 4.0 as a comparison, but the frequencies were systematically underestimated in the whole range. The frequencies are eigenvalues of the Hessian matrix, whose elements are the second derivatives of energy with respect to the displacements. Thus, they are very sensitive to the accuracy of the potential energy surface. This is also the reason that makes Raman/IR spectroscopy a powerful tool in detecting local chemical environment changes.

3. RESULTS AND DISCUSSION

Characterization of α-$Li_3V_2(PO_4)_3$. The solid-state synthesis of α-$Li_3V_2(PO_4)_3$ was as described in full detail in the

Experimental and Theoretical Methods. The product was characterized with XRD and ESEM to determine the phase purity, crystal structure, and particle size. As shown in Figure 1a, the material can be indexed to the monoclinic space group $P2_1/n$. ESEM images (Figure 1b) reveal highly agglomerated particles ranging from 0.1 to 50 μm in size.

Comparison of Experimental and Theoretical Raman Spectra. From the symmetry-based analysis of α-$Li_3V_2(PO_4)_3$, the predicted number of normal modes is 237 with 120 of these normal modes being Raman-active; the remainder are IR-active.[7]

$$\Gamma_{\alpha\text{-}Li_3V_2(PO_4)_3} = 60A_g + 60B_g + 59A_u + 58B_u \qquad (1)$$

As with any centrosymmetric crystal, the IR active modes are Raman-inactive and vice versa. Any mode that respects centrosymmetry is IR-active. The Raman-active modes can be further labeled as A_g or B_g. A_g modes are invariant under all four symmetry operations of the C_{2h} point group, whereas B_g modes are invariant for two of the operations. By analyzing the symmetry of each Raman mode for α-$Li_3V_2(PO_4)_3$ with pyspglib,[25] all of the Raman modes were labeled. Some of the calculated Raman modes, along with their symmetry assignments, can be found in Table 1. A complete list of the calculated modes can be found in Table S1 (Supporting Information). The vibration modes corresponding to the 294.9, 599.7, 1055.3, and 1085.7 cm^{-1} assignments are represented as schemes shown in Figure S1 (Supporting Information).[26]
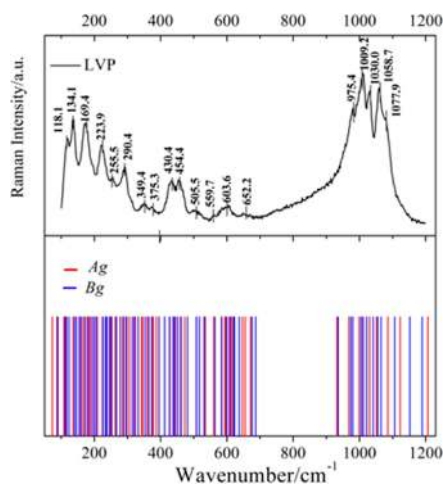
From the unpolarized Raman spectrum of α-$Li_3V_2(PO_4)_3$, only 19 vibrational modes, 1077.9, 1058.7, 1030.0, 1009.2, 975.4, 652.2, 603.6, 559.7, 505.5, 454.4, 430.4, 375.3, 349.4, 290.4, 255.5, 223.9, 169.4, 134.1, and 118.1 cm^{-1}, were detected (Figure 2 and Table 1).

Nevertheless, the DFT calculations clearly distinguish between the experimental spectral regions where vibrational modes occur from the regions where no vibrations are present. Vibrational spectra of transition-metal phosphates consist of internal and external modes. Internal modes are vibrations that occur within atomic groups (such as LiO_4, MO_6, and PO_4 polyhedra), and external modes are vibrations of the atomic groups and crystal lattice.[17] For the $Li_3M_2(PO_4)_3$ compounds, the PO_4 valency bond vibrations occur between 1250 and 900 cm^{-1}, PO_4 deformation vibrations are in the 700−400 cm^{-1} region, and the external lattice vibrations correspond to the

Table 1. Raman Modes for $Li_3V_2(PO_4)_3$ Observed by Raman Microscopy and the Corresponding Calculated Raman Modes with Symmetry Assignments by VASP-DFT

Raman vibrational modes for $Li_3V_2(PO_4)_3$ in units of cm^{-1}			
number	calculated	observed	assignment
1	1085.7	1077.9	A_g
2	1055.3	1058.7	B_g
3	1030.4	1030.0	A_g
4	1010.2	1009.2	A_g
5	974.0	975.4	A_g
6	654.9	652.2	A_g
7	599.7	603.6	B_g
8	560.4	559.7	A_g
9	508.0	505.5	B_g
10	451.2	454.4	B_g
11	427.5	430.4	B_g
12	376.5	375.3	A_g
13	346.1	349.4	A_g
14	294.9	290.4	A_g
15	252.7	255.5	A_g
16	224.3	223.9	A_g
17	167.6	169.4	A_g
18	136.2	134.1	A_g
19	116.7	118.1	B_g

Figure 2. Observed (top) and calculated (bottom) Raman spectra for α-$Li_3V_2(PO_4)_3$ in the 50–1230 cm^{-1} wavenumber range. The observed spectrum above was acquired with a 50× objective at a power of 0.855 mW and a total acquisition time of 120 s at room temperature.

low-frequency region of 400–0 cm^{-1}. As expected, the PO_4 valency bond vibrations are the most intense peaks.

Vibrational Modes of α-$Li_3V_2(PO_4)_3$ as a Function of Laser Irradiation Power. Raman spectra of α-$Li_3V_2(PO_4)_3$ were taken at different laser irradiation power to examine the phase stability of the material. At 0.067 mW, peaks centered at 1058.7, 1030.0, 1009.2, 975.4, 603.6, 454.4, 430.4, 290.4, 223.9, 169.4, and 134.1 cm^{-1} were detected, as is shown in Figure 3a. At 0.113 mW, additional peaks at 1077.9, 652.2, 559.7, 505.5, 375.3, 349.4, 255.5, and 118.1 cm^{-1} were detected. A gradual increase in power to 0.855 mW resulted in these peaks becoming sharper and more intense with no additional features appearing in any of the spectra (Figure 3a). Therefore, it was

concluded that, within the 0.067–0.855 mW power range, the monoclinic phase was conserved.

Irradiation at 0.855–4.101 mW resulted in various changes of the Raman spectrum (Figure 3b,c). Because spectral changes occurred rapidly, the acquisition time was reduced 6-fold in this power range. Within the first scan (20 s), the originally sharp phosphate vibrations in the high region of the spectrum were replaced with two broad peaks at 1048 and 1001 cm^{-1}. Two originally distinct peaks at 454.4 and 430.3 cm^{-1} merged into a single peak. Additionally, a shoulder around 1130 cm^{-1} emerged and the lattice vibrations significantly diminished in intensity. By the fifth scan (Figure 3b), the shoulder at 1130 cm^{-1} continued to grow in intensity and experienced a slight blue shift. Two new peaks were found at 947 and 876 cm^{-1}. After 220 s (11 scans), the new features of the spectrum stabilized (the shoulder at 1130 cm^{-1} was now further blue shifted to 1140 cm^{-1}). To determine whether the features of the stabilized spectrum were irreversible, the power was reduced to 0.855 mW. After seven scans, none of the general features changed (Figure S2a, Supporting Information). Therefore, only one scan was conducted at the lower irradiation power of 0.403 and 0.113 mW (Figure S2b, Supporting Information). Clearly, the original spectrum was not recovered.

Continuous irradiation at 4.101 mW caused the 876 cm^{-1} mode to dramatically increase in intensity (Figure 3d, i and ii). At the highest irradiation power of 7.612 mW, the intensity of the 876 cm^{-1} peak dominated the remaining spectral features of the spectrum (Figure 3d). Moreover, visually the original green powder became a much darker, olive green. Evidently, α-$Li_3V_2(PO_4)_3$ is not stable at an irradiation power of 4.101 mW or greater.

Similar power studies have been conducted on olivine $LiFePO_4$. Bai et al.[27] showed that the thermal effect of laser irradiation created two new peaks in the low-wavenumber region at 215 and 277 cm^{-1}. These peaks were associated with formation of α-Fe_2O_3.[28] Continual laser irradiation led to a broad background in the high-wavenumber region that the authors attributed to amorphous $FePO_4$. However, upon reversing the power of the laser, the amorphous background vanished and the most prominent peak centered at 950 cm^{-1} remained unchanged in intensity, showing that the basic structure was maintained throughout the course of the study. It could be assumed that comparable transformations occurred for α-$Li_3V_2(PO_4)_3$, possibly leading to the creation of V_2O_5 and amorphous $V_2(PO_4)_3$. The formation of these phase impurities created by laser irradiation on $Li_3V_2(PO_4)_3$ were indirectly investigated through thermal studies.

Thermal Studies on α-$Li_3V_2(PO_4)_3$. In the confocal Raman microscope arrangement, a very high power density is concentrated on a small area of the sample. Absorption of radiation can cause the local temperature to increase by several hundreds of degrees. Consequently, as the irradiation power was increased, the local temperature of α-$Li_3V_2(PO_4)_3$ also increased. Having conducted the measurements in air, it is reasonable to suspect that the material is susceptible to oxidation at the higher irradiation power and that oxidation brought about the changes in the Raman spectrum. In situ Raman heat treatment in air and in an inert atmosphere (N_2) clarified this using a temperature-controlled heating stage.

A microscope heating stage permitted the acquisition of Raman spectra for α-$Li_3V_2(PO_4)_3$ from room temperature to 600 °C. No spectral changes were observed from 23.5 to 116.7 °C (Figure 4a), indicating that the monoclinic phase was
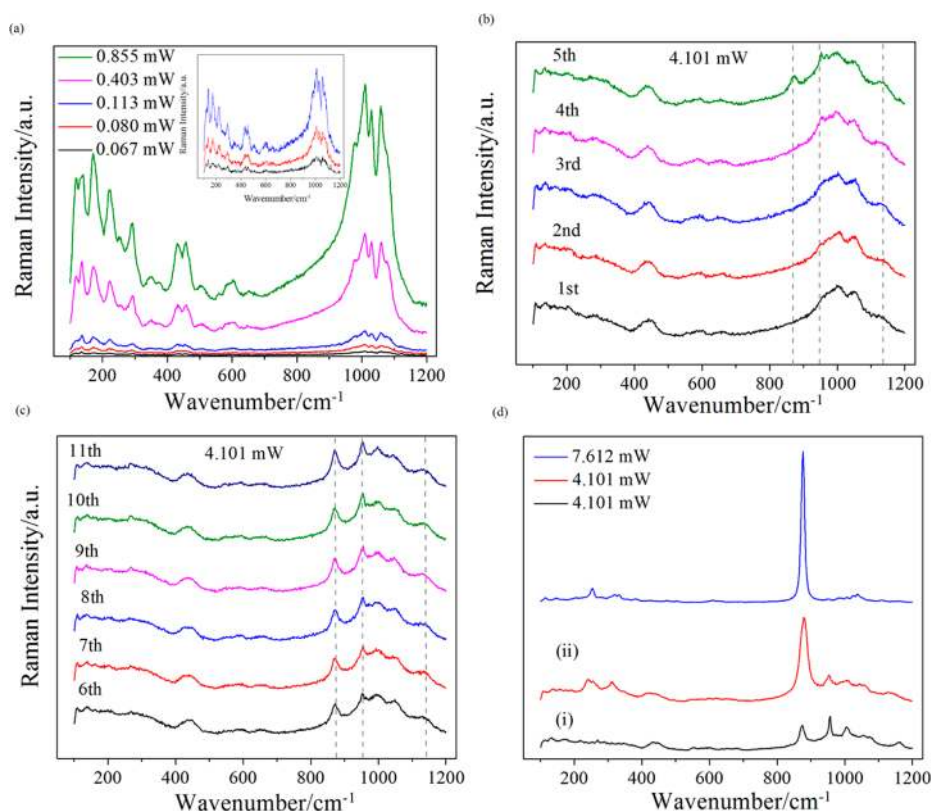
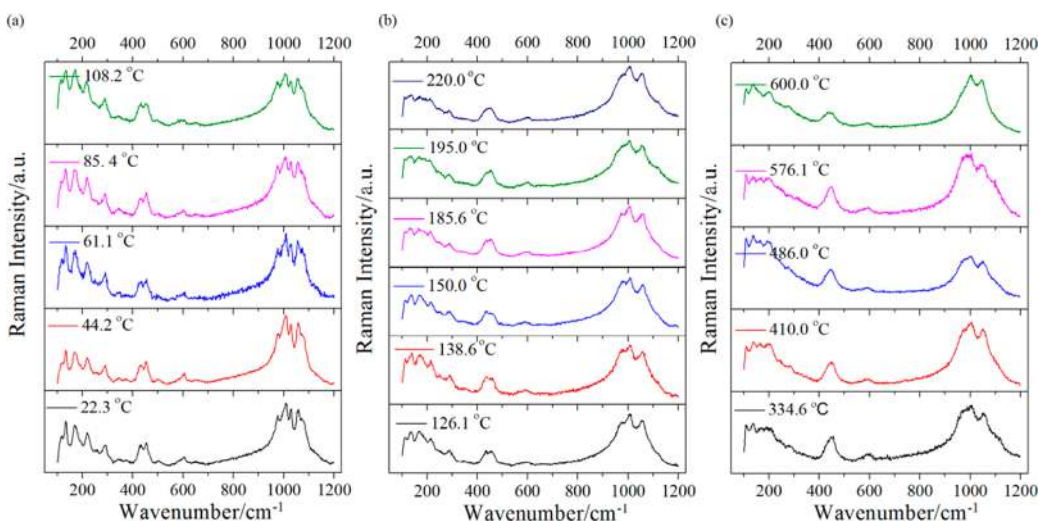**Figure 3.** Raman spectra of α-Li$_3$V$_2$(PO$_4$)$_3$ at different laser irradiation power with the 50× objective: (a) from 0.067 to 0.855 mW (120 s acquisition time), (b, c) 11 successive measurements at 4.101 mW, with each acquisition being 20 s, (d) continuous exposure at 4.101 mW with longer acquisitions of (i) 120 s and (ii) 300 s and the highest power measurement at 7.612 mW (120 s acquisition time).
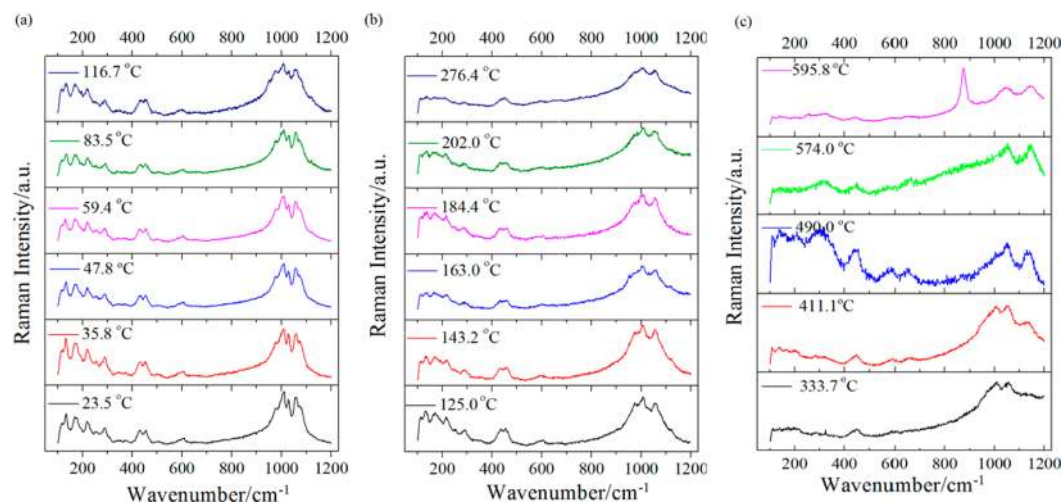
Figure 4. In situ Raman spectra of α-Li$_3$V$_2$(PO$_4$)$_3$ at different heating temperatures under air: (a) from 23.5 to 116.7 °C, (b) 125.0 to 276.4 °C, and (c) 333.7 to 595.8 °C taken with a 50× objective and a laser power of 0.855 mW for 300 s.

preserved in air within this temperature range. At 125 °C, the 1030 cm^{-1} peak and shoulder at 1079 cm^{-1} disappeared. These general features remained until reaching 202.0 °C, at which point more dramatic changes took place, such as broadening of the 1009 cm^{-1} peak, merging of the 435 and 455 cm^{-1} peaks into a single peak, transformation of the 979 cm^{-1} peak into a shoulder, and a significant diminishing of the lattice modes. The general features of the spectrum at 202.0 °C (Figure 4b) closely matched those of the first scan at a power of 4.101 mW in the irradiation power study (Figure 3b).

A further increase in heating temperature (Figure 4c) resulted in additional spectral changes. At 333.7 °C, an additional peak at 1140 cm^{-1} can be seen that gradually grew in intensity with higher heating temperatures and experienced a slight blue shift once reaching 595.8 °C. Furthermore, at 595.8 °C, a new peak at 876 cm^{-1} became the dominant mode of the spectrum. These changes are analogous to the spectral transitions seen during the irradiation power study (Figure S3a,b, Supporting Information). However, the lower intensity of the 876 cm^{-1} mode at 595.8 °C as compared to the spectrum at 7.612 mW indicated two things: the local temperature of the

**Figure 5.** In situ Raman spectra of α-Li$_3$V$_2$(PO$_4$)$_3$ at different temperatures under N$_2$: (a) from 22.3 to 108.2 °C, (b) 126.1 to 220.0 °C, and (c) 334.6 to 600.0 °C taken with a 50× objective and a laser power of 0.855 mW for 300 s.

sample under 7.612 mW power was greater than 600 °C, and at 600 °C, the material was not completely oxidized.

The in situ Raman heating experiment was repeated under a N$_2$ atmosphere. This experiment was done to confirm that α-Li$_3$V$_2$(PO$_4$)$_3$ underwent oxidation under either elevated temperatures or irradiation power in air and to distinguish any spectral, and therefore structural changes, that could be unrelated to the oxidation reaction. Such structural changes include transformation of lattice symmetry, cell expansion/contraction, and atomic disordering. Under N$_2$, the monoclinic phase is also retained within the 22.3−108.2 °C temperature range (Figure 5a). Again, no appreciable peak broadening is noted. As in the heating experiment conducted in air, at 126.1 °C, the 1030 cm^{-1} peak and shoulder at 1079 cm^{-1} disappeared. The same spectral characteristics detected at 202.0 °C in air were detected at 195.0 °C in N$_2$, which included broadening of the 1009 cm^{-1} peak, merging of the 435 and 455 cm^{-1} modes into a single peak, transformation of the 979 cm^{-1} peak into a shoulder, and lowered intensity of the lattice modes (Figure 5b). Increasing the temperature from 195.0 to 600.0 °C resulted in no further changes in the spectrum (Figure 5c). When the material was subsequently cooled down to room temperature, the Raman spectrum exactly matched that of the initial α-Li$_3$V$_2$(PO$_4$)$_3$ (Figure S4, Supporting Information).

Li$_3$V$_2$(PO$_4$)$_3$ is isotypic with Li$_3$M$_2$(PO$_4$)$_3$, where M = Fe, Sc. These crystals are found in the α-phase at room temperature and exhibit two structural phase changes at elevated temperatures (β and γ).[29−31] In the $\alpha \rightarrow \beta$ transition, the MO$_6$ octahedra and PO$_4$ tetrahedra show a slightly higher symmetry, but the greatest distinction in the structure is the Li ion arrangement.[29] In the α-phase, Li ions are located in three unique positions, Li(1), Li(2), and Li(3). The least energetically favorable, Li(3), is repositioned to a new location, Li(1s), which is related in symmetry to Li(1). During the high-temperature transition from $\beta \rightarrow \gamma$, more notable structural transformations occur. The MO$_6$ octahedra and PO$_4$ tetrahedra 3-D framework converts from the monoclinic to the orthorhombic structure, and all of the Li ions are rearranged. The 12 Li ions of the unit cell are repositioned over three new crystallographic positions where two of the positions are only partially occupied. It is expected that α-Li$_3$V$_2$(PO$_4$)$_3$ also undergoes similar intermediate and high-temperature phase

transitions. Differential scanning calorimetry (DSC) studies of α-Li$_3$V$_2$(PO$_4$)$_3$ were completed from 25 to 250 °C and then back to 25 °C for a total of three cycles. The first cycle was used to remove any adsorbed water from the material, and the next two cycles were completed to determine the reversibility of the phases. As shown in Figure 6, two structural modifications
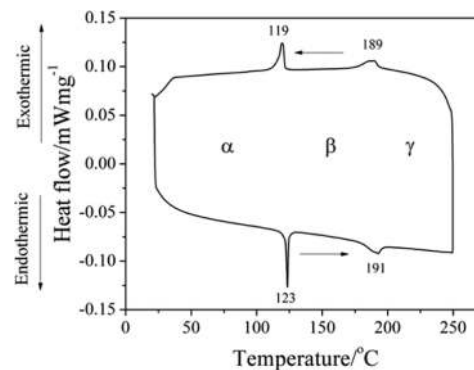

Figure 6. DSC curve of α-Li$_3$V$_2$(PO$_4$)$_3$ from 25 to 250 °C at a rate of 5 °C/min under a N$_2$ flow rate of 50.00 mL/min.

occur at roughly 123 °C (β-phase) and 191 °C (γ-phase).[28,29] All of the phase transitions were reversible upon cooling back to room temperature (Figure 6, and Figure S5a,b, Supporting Information).

From the DSC plot, the temperature for the crystalline phase changes of Li$_3$V$_2$(PO$_4$)$_3$ occurred at 123 °C ($\alpha \rightarrow \beta$) and 191 °C ($\beta \rightarrow \gamma$), and from 191 °C and greater, the γ-phase is predominant. Undeniably, these crystalline phase changes are responsible for the Raman spectral changes between 23 and 200 °C under N$_2$ and air (Figure 7). However, in situ XRD data provided by Bykov et al.[29] have shown evidence of high-temperature twinning of $\alpha + \beta$, $\beta + \gamma$, and even of all three phases at once. Therefore, the spectra in Figure 7 may not exclusively represent a single phase. In the $\beta \rightarrow \gamma$ transition, there is a more drastic change in structure as compared to the $\alpha \rightarrow \beta$ transition. From the Raman spectral changes of the phases, the opposite would be expected. Twinning of the phases could explain why the structural and Raman trends do not follow.
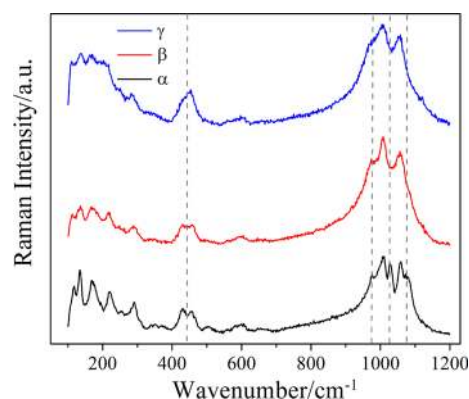
Figure 7. Raman spectra of the α, β, and γ crystalline phases for α-$Li_3V_2(PO_4)_3$ under N_2.

No crystallographic phase transitions for $Li_3V_2(PO_4)_3$ occurred past 200 °C. Therefore, any Raman spectral changes past this temperature in air must have been induced by oxidation. To prove this hypothesis, TGA under an air flow was used to monitor the weight change of $Li_3V_2(PO_4)_3$ from 25 to 800 °C (Figure 8a). The original 4.437 mg sample initially lost 0.024 mg, corresponding to the evaporation of adsorbed water. After 330 °C, the material began to oxidize, and by 800 °C, it had an ~4% increase in mass.[32] In this case, the originally loose, green powder had sintered into a single, large, olive-colored particle.

XRD was conducted thereafter to determine phase impurities. No V_2O_5 was detected. Instead, the material was found to be triclinic $LiVOPO_4$ ($P\bar{1}$ space group) with no $Li_3V_2(PO_4)_3$ detected from the pattern (Figure 8b). The Raman spectrum included vibrational modes at 1116, 1039,

1028, 993, 956, 685, 615, 536, 332, 255, 148, and 119 cm^{-1} (Figure 8c). To the best of our knowledge, no Raman literature exists for triclinic α-$LiVOPO_4$. Raman data are, however, reported for rhombohedral β-$LiVOPO_4$.[33] Qualitatively speaking, the spectrum for β-$LiVOPO_4$ correlates well with the Raman spectrum of the oxidized $Li_3V_2(PO_4)_3$ material. The two spectra share the dominating spectral feature as an intense peak close to ~880 cm^{-1} that Baran et al.[33] assigned to the V═O stretching mode. However, the possibility of low concentrations for the partially delithiated phases $Li_{3-x}V_2(PO_4)_3$, $0 < x < 3$, possibly undetectable by XRD, cannot be ruled out. Interestingly, Kuo et al.[34] found through in situ XRD studies that α-$LiVOPO_4$ transforms into α-$Li_3V_2(PO_4)_3$ at temperatures above 600 °C under a reducing atmosphere. The present work has identified a new reaction. α-$Li_3V_2(PO_4)_3$ transforms into α-$LiVOPO_4$ at temperatures above 600 °C in an oxidizing atmosphere.

Understanding the behavior of a species under laser irradiation and heating is critical for correct interpretation of micro-Raman experiments. Previously, Burba et al.[7] conducted Raman vibrational studies of α-$Li_3V_2(PO_4)_3$ in the hopes of conducting in situ spectroelectrochemical measurements of this material. This study was particularly interested in following the high-frequency region of the spectrum assigned to PO_4 valency stretching modes, which are the most intense peaks in the spectrum. However, there were only four weak bands detected in the 1200−850 cm^{-1} region at 1142, 1055, 1011, and 973 cm^{-1}. The spectrum of α-$Li_3V_2(PO_4)_3$ at 411.1 °C also shows similarly broad peaks at 1138, 1053, 1005, and 977 cm^{-1} (Figure 5c). It is reasonable to suspect that the features found by Burba et al.[7] correspond to thermal degradation of the α-phase into the γ-phase, with the peak at 1138 cm^{-1} indicating oxidation.
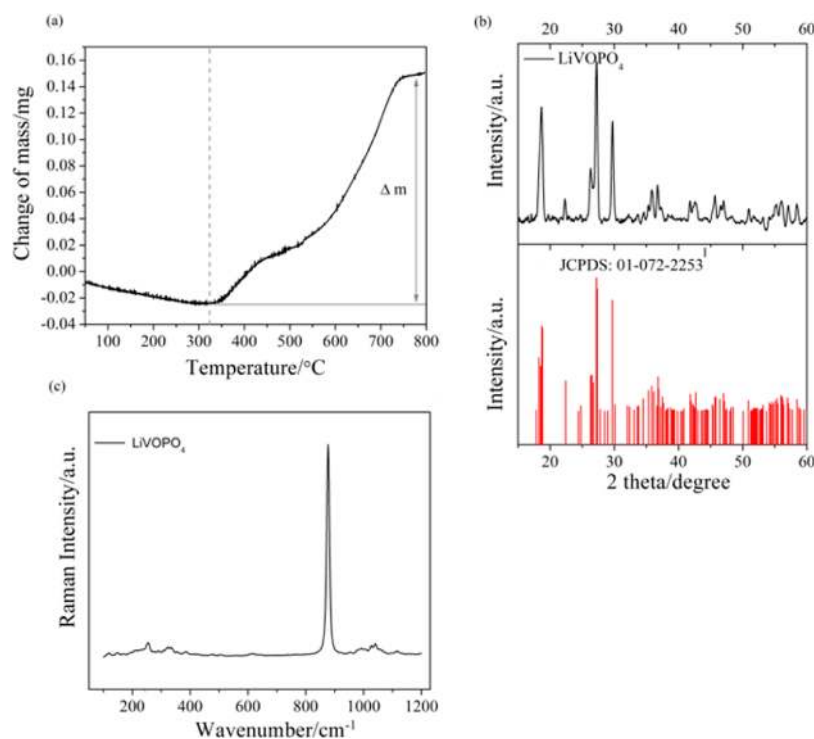
Figure 8. (a) TGA curve of α-$Li_3V_2(PO_4)_3$ under air from 25 to 800 °C. The first ramp was from 25 to 500 °C at a rate of 2.50 °C/min. The second ramp continued heating from 500 to 800 °C at a rate of 5.00 °C/min. (b) XRD and (c) Raman of the sample after the TGA analysis with the 50× objective at a power of 0.855 mW with a 120 s acquisition time identifying α-$LiVOPO_4$ as the product of oxidation.

4. CONCLUSIONS

In this paper, we report the experimental Raman spectrum, along with the corresponding theoretical Raman spectrum and symmetry assignments for α-Li$_3$V$_2$(PO$_4$)$_3$ by DFT. Experimentally, only 19 of the 120 Raman modes predicted by factor group analysis were identified. As anticipated, the internal phosphate stretching modes located in the high-frequency region contain the sharpest and most intense peaks, making it the prevailing feature of the spectrum. Like LiFePO$_4$, Li$_3$V$_2$(PO$_4$)$_3$ is unstable under certain laser irradiation power ($\sim\geq$4 mW) caused by rapid heating and a temperature increase under micro-Raman measurements. From our Raman and thermal measurements, it was found that the monoclinic phase experiences two thermally induced structural transformations to the β- and γ-phases analogous to its isostructural counterparts, Li$_3$Sc$_2$(PO$_4$)$_3$ and Li$_3$Fe$_2$(PO$_4$)$_3$. Continuous heating under air results in oxidation of α-Li$_3$V$_2$(PO$_4$)$_3$ to α-LiVOPO$_4$. These experiments provide fundamental groundwork for future in situ Raman studies of α-Li$_3$V$_2$(PO$_4$)$_3$ as a cathode for lithium-ion storage devices.

■ ASSOCIATED CONTENT

Ⓢ Supporting Information

A table and five figures are provided as mentioned in the text. This material is available free of charge via the Internet at http://pubs.acs.org.

■ AUTHOR INFORMATION

Corresponding Author

*Phone: + 1-512-232-9160 (K.J.S.), + 1-512-471-4179 (G.H.). Fax: + 1-512-471-8696 (K.J.S.), + 1-512-471-8696 (G.H.). E-mail: stevenson@cm.utexas.edu (K.J.S.), henkelman@mail.utexas.edu (G.H.).

Notes

The authors declare no competing financial interest.

■ ACKNOWLEDGMENTS

■ REFERENCES

(1) Yuan, L.-X.; Wang, Z.-H.; Zhang, W.-X.; Hu, X.-L.; Chen, J.-T.; Huang, Y.-H.; Goodenough, J. B. Development and Challenges of LiFePO$_4$ Cathode Material for Lithium-Ion Batteries. *Energy Environ. Sci.* **2011**, *4*, 269−284.

(2) Yin, S.-C.; Grondey, H.; Strobel, P.; Anne, M.; Nazar, L. F. Electrochemical Property: Structure Relationships in Monoclinic Li$_3$V$_2$(PO$_4$)$_3$. *J. Am. Chem. Soc.* **2003**, *125*, 10402−10411.

(3) Huang, H.; Yin, S.-C.; Kerr, T.; Taylor, N.; Nazar, L. F. Nanostructured Composites: A High Capacity, Fast Rate Li$_3$V$_2$-(PO$_4$)$_3$/Carbon Cathode for Rechargeable Lithium Batteries. *Adv. Mater.* **2002**, *14*, 1525−1528.

(4) Lee, S.; Park, S. S. Atomistic Simulation Study of Monoclinic Li$_3$V$_2$(PO$_4$)$_3$ as a Cathode Material for Lithium Ion Battery: Structure, Defect Chemistry, Lithium Ion Transport Pathway, and Dynamics. *J. Phys. Chem. C* **2012**, *116*, 25190−25197.

(5) Baddour-Hadjean, R.; Pereira-Ramos, J.-P. Raman Microspectrometry Applied to the Study of Electrode Materials for Lithium Batteries. *Chem. Rev.* **2009**, *110*, 1278−1319.

(6) Morcrette, M.; Leriche, J.-B.; Patoux, S.; Wurm, C.; Masquelier, C. In Situ X-Ray Diffraction During Lithium Extraction from Rhombohedral and Monoclinic Li$_3$V$_2$(PO$_4$)$_3$. *Electrochem. Solid-State Lett.* **2003**, *6*, A80−A84.

(7) Burba, C. M.; Frech, R. Vibrational Spectroscopic Studies of Monoclinic and Rhombohedral Li$_3$V$_2$(PO$_4$)$_3$. *Solid State Ionics* **2007**, *177*, 3445−3454.

(8) Shu, J.; Shui, M.; Xu, D.; Gao, S.; Yi, T.; Wang, D. J.; Li, X.; Ren, Y. Design and Comparison of Ex Situ and In Situ Devices for Raman Characterization of Lithium Titanate Anode Material. *Ionics* **2011**, *17*, 503−509.

(9) Burba, C. M.; Frech, R. Modified Coin Cells for In Situ Raman Spectroelectrochemical Measurements of Li$_x$V$_2$O$_5$ for Lithium Rechargeable Batteries. *Appl. Spectrosc.* **2006**, *60*, 490−493.

(10) Kim, Y. A.; Kojima, M.; Muramatsu, H.; Umemoto, S.; Watanabe, T.; Yoshida, K.; Sato, K.; Ikeda, T.; Hayashi, T.; Endo, M.; Terrones, M.; Dresselhaus, M. S. In Situ Raman Study on Single- and Double-Walled Carbon Nanotubes as a Function of Lithium Insertion. *Small* **2006**, *2*, 667−676.

(11) Cahill, L. S.; Chapman, R. P.; Britten, J. F.; Goward, G. R. ^{7}Li NMR and Two-Dimensional Exchange Study of Lithium Dynamics in Monoclinic Li$_3$V$_2$(PO$_4$)$_3$. *J. Phys. Chem. B* **2006**, *110*, 7171−7177.

(12) Yin, S.-C.; Grondey, H.; Strobel, P.; Huang, H.; Nazar, L. F. Charge Ordering in Lithium Vanadium Phosphates: Electrode Materials for Lithium-Ion Batteries. *J. Am. Chem. Soc.* **2002**, *125*, 326−327.

(13) Patoux, S.; Wurm, C.; Morcrette, M.; Rousse, G.; Masquelier, C. A Comparative Structural and Electrochemical Study of Monoclinic Li$_3$Fe$_2$(PO$_4$)$_3$ and Li$_3$V$_2$(PO$_4$)$_3$. *J. Power Sources* **2003**, *119−121*, 278−284.

(14) Burba, C. M.; Frech, R. Raman and FTIR Spectroscopic Study of Li$_x$FePO$_4$ ($0 \leq x \leq 1$). *J. Electrochem. Soc.* **2004**, *151*, A1032−A1038.

(15) Barj, M.; Lucazeau, G.; Delmas, C. Raman and Infrared Spectra of Some Chromium Nasicon-Type Materials: Short-Range Disorder Characterization. *J. Solid State Chem.* **1992**, *100*, 141−150.

(16) Butt, G.; Sammes, N.; Tompsett, G.; Smirnova, A.; Yamamoto, O. Raman Spectroscopy of Superionic Ti-Doped Li$_3$Fe$_2$(PO$_4$)$_3$ and LiNiPO$_4$ Structures. *J. Power Sources* **2004**, *134*, 72−79.

(17) Kravchenko, V. V.; Mikhailov, V. I.; Sigarev, S. E. Some Features of Vibrational Spectra of Li$_3$M$_2$(PO$_4$)$_3$ (M = Sc, Fe) Compounds Near a Superionic Phase Transiton. *Solid State Ionics* **1992**, *50*, 19−30.

(18) Paraguassu, W.; Freire, P. T. C.; Lemos, V.; Lala, S. M.; Montoro, L. A.; Rosolen, J. M. Phonon Calculation on Olivine-like LiMPO$_4$ (M = Ni, Co, Fe) and Raman Scattering of the Iron-Containing Compound. *J. Raman Spectrosc.* **2005**, *36*, 213−220.

(19) Kohn, W.; Becke, A. D.; Parr, R. G. Density Functional Theory of Electronic Structure. *J. Phys. Chem.* **1996**, *100*, 12974−12980.

(20) Heyd, J.; Scuseria, G. E.; Ernzerhof, M. Hybrid Functionals Based on a Screened Coulomb Potential. *J. Chem. Phys.* **2003**, *118*, 8207−8215.

(21) Kresse, G.; Furthmüller, J. Efficiency of Ab-Initio Total Energy Calculations for Metals and Semiconductors Using a Plane-Wave Basis Set. *Comput. Mater. Sci.* **1996**, *6*, 15−50.

(22) Kresse, G.; Furthmüller, J. Efficient Iterative Schemes for *Ab Initio* Total-Energy Calculations Using a Plane-Wave Basis Set. *Phys. Rev. B* **1996**, *54*, 11169−11186.

(23) Blöchl, P. E. Projector Augmented-Wave Method. *Phys. Rev. B* **1994**, *50*, 17953−17979.

(24) Kresse, G.; Joubert, D. From Ultrasoft Pseudopotentials to the Projector Augmented-Wave Method. *Phys. Rev. B* **1999**, *59*, 1758−1775.

(25) pyspglib for ASE; **2013**. http://spglib.sourceforge.net/pyspglibForASE/ (Accessed February 15, 2013).

(26) Canepa, P.; Hanson, R. M.; Ugliengo, P.; Alfredsson, M. J-ICE: A New Jmol Interface for Handling and Visualizing Crystallographic and Electronic Properties. *J. Appl. Crystallogr.* **2011**, *44*, 225−229.

(27) Bai, Y.; Yin, Y.; Yang, J.; Qing, C.; Zhang, W. Raman Study of Pure, C-Coated and Co-Doped $LiFePO_4$: Thermal Effect and Phase Stability Upon Laser Heating. *J. Raman Spectrosc.* **2011**, *42*, 831−838.

(28) Shebanova, O. N.; Lazor, P. Raman Study of Magnetite (Fe_3O_4): Laser-Induced Thermal Effects and Oxidation. *J. Raman Spectrosc.* **2003**, *34*, 845−852.

(29) Bykov, A. B.; Chirkin, A. P.; Demyanets, L. N.; Doronin, S. N.; Genkina, E. A.; Ivanov-Shits, A. K.; Kondratyuk, I. P.; Maksimov, B. A.; Mel'nikov, O. K.; Muradyan, L. N.; Simonov, V. I.; Timofeeva, V. A. Superionic Conductors Lithium Metal Phosphate ($Li_3M_2(PO_4)_3$)(M = Fe, Sc, Cr): Synthesis, Structure and Electrophysical Properties. *Solid State Ionics* **1990**, *38*, 31−52.

(30) Ohkawa, H.; Yoshida, K.; Saito, M.; Uematsu, K.; Toda, K.; Sato, M. Improvement of Discharge Capacity of β-$Fe_2(SO_4)_3$-Type $Li_3V_2(PO_4)_3$ by Stabilizing High Temperature Orthorhombic Phase at Room Temperature. *Chem. Lett.* **1999**, *28*, 1017−1018.

(31) Sato, M.; Ohkawa, H.; Yoshida, K.; Saito, M.; Uematsu, K.; Toda, K. Enhancement of Discharge Capacity of $Li_3V_2(PO_4)_3$ by Stabilizing the Orthorhombic Phase at Room Temperature. *Solid State Ionics* **2000**, *135*, 137−142.

(32) Kuang, Q.; Zhao, Y.; An, X.; Liu, J.; Dong, Y.; Chen, L. Synthesis and Electrochemical Properties of Co-Doped $Li_3V_2(PO_4)_3$ Cathode Materials for Lithium-Ion Batteries. *Electrochim. Acta* **2010**, *55*, 1575−1581.

(33) Baran, E. J.; Vassallo, M. B.; Lii, K. H. Vibrational Spectra of β-$LiVOPO_4$ and $NaVOPO_4$. *J. Raman Spectrosc.* **1994**, *25*, 199−202.

(34) Kuo, H. T.; Bagkar, N. C.; Liu, R. S.; Shen, C. H.; Shy, D. S.; Xing, X. K.; Lee, J.-F.; Chen, J. M. Structural Transformation of $LiVOPO_4$ to $Li_3V_2(PO_4)_3$ with Enhanced Capacity. *J. Phys. Chem. B* **2008**, *112*, 11250−11257.